Higher-Order Fabry-Pérot Interferometer from Topological Hinge States

Chang-An Li,[1,*] Song-Bo Zhang,[1,†] Jian Li,[2,3] and Björn Trauzettel[1,4]
[1]*Institute for Theoretical Physics and Astrophysics, University of Würzburg, 97074 Würzburg, Germany*
[2]*School of Science, Westlake University, 18 Shilongshan Road, Hangzhou 310024, Zhejiang Province, China*
[3]*Institute of Natural Sciences, Westlake Institute for Advanced Study,*
18 Shilongshan Road, Hangzhou 310024, Zhejiang Province, China
[4]*Würzburg-Dresden Cluster of Excellence ct.qmat, Germany*

(Received 19 January 2021; revised 23 April 2021; accepted 9 June 2021; published 8 July 2021)

We propose an intrinsic three-dimensional Fabry-Pérot type interferometer, coined “higher-order interferometer,” that is based on the chiral hinge states of second-order topological insulators and *cannot* be mapped to an equivalent two-dimensional setting because of higher-order topological obstructions. Quantum interference patterns in the two-terminal conductance of this interferometer are controllable not only by tuning the strength but also, particularly, by rotating the direction of the magnetic field applied perpendicularly to the transport direction. Remarkably, the conductance exhibits a characteristic beating pattern with multiple frequencies depending on the field strength and direction in a unique fashion. Our novel interferometer thus provides feasible and robust magnetotransport signatures for hinge states of higher-order topological insulators.

DOI: 10.1103/PhysRevLett.127.026803

Introduction.—Higher-order topological insulators (HOTIs) feature gapless excitations, similar to conventional (first-order) topological insulators, that are protected by the nontrivial topology of bulk electronic bands but localized at open boundaries at least two dimensions lower than the insulating bulk [1–16]. For instance, three-dimensional (3D) second-order topological insulators (SOTIs) host one-dimensional chiral or helical states along specific hinges of the samples inside their topological gaps. The recent discoveries of HOTIs in a variety of candidate systems have not only extended our understanding of topological phases of matter but also inspired wide-ranging potential applications [17–44]. Whereas most of the research efforts so far have been put into the electronic structures of potential HOTI material, their transport properties remain largely unexplored despite some investigations involving superconductivity [45–47]. Indeed, an intriguing open question regarding 3D SOTIs in particular is whether there exist unique transport effects that can unambiguously detect topological hinge states and further lead to their functionalization.

One appealing route toward addressing this question involves interferometry built upon 3D SOTIs, or more precisely, through quantum-coherent transport via the hinge states. Propagating hinge states that form an interference loop can enclose a magnetic flux applied to the system and thereby pick up an Aharonov-Bohm (AB) phase [48]. In the presence of quantum coherence, the AB phase will give rise to quantum oscillations in transport characteristics such as charge conductance. Quantum interference patterns in the conductance of two-terminal devices have been routinely employed to detect topological states such as surface states of topological insulators [49–52], chiral Majorana modes [53–56], and topological Dirac semimetals [57].

In this Letter, we propose a higher-order Fabry-Pérot interferometer based on hinge states of SOTIs. Our basic setup, shown in Fig. 1(a), consists of a chiral SOTI in contact with two metallic leads. The chiral hinge states, combined with partial reflections at the SOTI and lead interfaces, form interference loops that are interconnected in 3D space. Under external magnetic fields, the two-terminal conductance in this setup exhibits peculiar quantum interference patterns originating from the AB effect and tunable by both field strength and orientation, as exemplified by Fig. 1(c). Owing to the inherent 3D nature of the interferometer, there are generally two linked frequencies in the magnetoconductance oscillations, leading to a beating pattern. When varying the magnetic field direction, one frequency increases while the other decreases and they cross at certain field directions. These features are independent of the details of the device and stable against moderate disorder and dephasing. Hence, they provide robust transport signatures of hinge states in 3D SOTIs [58].

General analysis by scattering-matrix theory.—Before presenting microscopic models, it is instructive to analyze the main transport features of the interferometer using a phenomenological scattering approach [59–61]. For simplicity, we assume that the hinge states in our setup are well separated by the insulating bulk and side surfaces such that scattering only occurs at the interfaces between normal metal leads and the SOTI sample [Fig. 1(a)]. This also

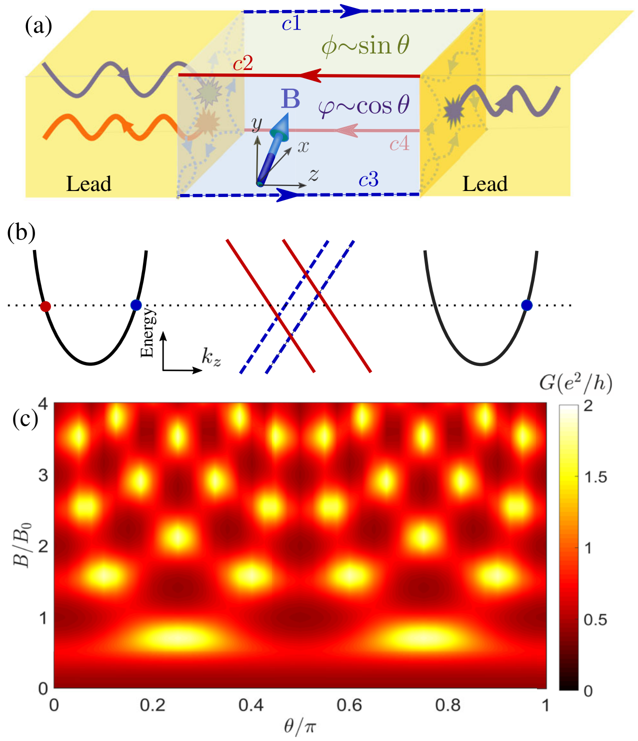

FIG. 1. (a) Schematic of the higher-order interferometer: SOTI with four chiral hinge states (solid red and dashed blue lines) connected to two leads. A magnetic field $\mathbf{B}$ is applied perpendicularly to the z direction in the SOTI with strength B and an angle θ with respect to $+x$ axis. The dotted arrow lines at the interfaces indicate the scattering between the hinge states. (b) Sketch of the low-energy spectra in three regions in (a) with the Fermi energy indicated by the dotted line. The leads have a parabolic spectrum, and the SOTI has a linear spectrum split by $\mathbf{B}$. (c) Density plot of conductance against B and θ. $B_0 = \phi_0/S_f$ with ϕ_0 the flux quantum and S_f the area of the front surface of the SOTI.

implies that the possible gapless states on the two terminal surfaces, which become part of the interfaces, will not affect our following analysis as we will consider generic scattering matrix elements for these interfaces. Consider electrons (blue wavy line) coming from the left lead [Fig. 1(a)]. The incident electrons first experience reflection (red wavy line) or transmission (characterized by a transmission matrix t_L) into the right-moving hinge channels $c1$ and $c3$ (blue dashed lines) at the left interface. The transmitted electrons propagate along $c1$ and $c3$ forward to the right interface. Then, they again experience partial reflection (described by r_R) back into the left-moving hinge channels $c2$ and $c4$ (red solid lines), and partial transmission (described by t_R) into the right lead (blue wavy line). The reflected electrons in $c2$ and $c4$ go backward and are partially reflected (described by $r_{L'}$) at the left interface into $c1$ and $c3$. Because of the finite reflections at the interfaces, electrons propagating along the hinges of the SOTI undergo multiple reflections at the interfaces before exiting to the leads, and their trajectory inside the SOTI forms closed loops. In this sense, we have a Fabry-Pérot interferometer.

In the presence of a magnetic field $\mathbf{B} = B(\cos\theta, \sin\theta, 0)$ with strength B and direction θ, the trajectory loops in the SOTI can enclose magnetic fluxes. Thus, electrons propagating along these loops pick up AB phases. For instance, the loop involving $c1$ and $c2$ ($c2$ and $c3$) on the top (front) surface of Fig. 1(a) encloses a magnetic flux $\phi = BLW_x \sin\theta$ ($\varphi = BLW_y \cos\theta$), where L is the distance between the two leads and $W_{x/y}$ the width of the SOTI in the x/y direction. The scattering propagation of electrons in the hinge channels can be described by a 2×2 matrix [62],

$$\mathcal{S}(B,\theta) = e^{i\lambda/2} e^{i\Phi_+} (\mathbb{1} - e^{i\lambda} r_{L'} e^{i\Phi_-} r_R e^{i\Phi_+})^{-1}, \qquad (1)$$

where $\Phi_\pm = (\varphi \pm \phi)\sigma_z/2$ account for the AB phase differences between the two right-moving and between the two left-moving hinge channels, respectively; σ_z is the Pauli matrix acting on pseudospin space for two left- or right-moving hinge channels, and $\lambda = 2k_F L$ is the dynamical phase with k_F the Fermi wave number. The term with $r_{L'}$ and r_R in the denominator of Eq. (1) corresponds to the encircling processes in the SOTI, reflecting the multiple reflection properties of the Fabry-Pérot interferometer. The transmission matrix of the setup is then expressed as $t_R \mathcal{S}(B,\theta) t_L$. It indicates that the electrons transmit from one lead to the SOTIs (t_L), undergo multiple reflections [$\mathcal{S}(B,\theta)$], and finally transmit to the other lead (t_R). We provide more details of this analysis in the Supplemental Material (SM) [62].

With the transmission matrix, the conductance of the setup at zero temperature can be evaluated as

$$G(B,\theta) = \frac{e^2}{h} \mathrm{Tr}[t_R^\dagger t_R \mathcal{S}(B,\theta) t_L t_L^\dagger \mathcal{S}^\dagger(B,\theta)], \qquad (2)$$

where e^2/h is the conductance quantum. Clearly, G vanishes if there is no transmission across the interfaces, i.e., $t_L = 0$ or $t_R = 0$. G becomes quantized at $2e^2/h$ and independent of $\mathbf{B}$ if the interfaces are completely transparent, i.e., $r_{L'} = 0$ and $r_R = 0$. Otherwise, G generically depends on $\mathbf{B}$ via the phases φ and ϕ. Particularly, if we assume that the two interfaces are identical and the scattering is equally probable between leads and individual hinge channels as well as among hinge channels, i.e., $t_L = t_R = \sqrt{1-R}\mathbb{1}$ and $r_{L'} = -r_R = \sqrt{R/2}(\sigma_z + \sigma_x)$, we find explicitly

$$G = \frac{2e^2}{h} \frac{(1-R)^2[1 + R^2 + R\cos\lambda(\cos\phi + \cos\varphi)]}{|1 + R^2 e^{2i\lambda} + Re^{i\lambda}(\cos\phi + \cos\varphi)|^2}. \qquad (3)$$

These results indicate the necessary condition for a working interferometer: finite transmission and reflection at the interfaces for the hinge states. Note that this condition is common, for example, in the presence of a mismatch between transport channels across the interfaces, as shown in Fig. 1(b), or interface barriers.

Moreover, the matrix $\mathcal{S}$ contains explicitly two field-dependent phases $\varphi \pm \phi$ in general. This indicates the appearance of beating patterns with two linked frequencies in the magnetoconductance. Notably, the two frequencies are intimately connected to the magnetic fluxes threading the different side surfaces of the SOTI. They are solely determined by the geometry of the sample and insensitive to the details of the interface barriers. Since the dynamic phase λ in Eq. (1) is unchanged by magnetic fields, it does not affect our results qualitatively. We have verified these predictions by properly parameterizing the scattering matrices [62].

Model simulation and method.—To demonstrate these features explicitly, we consider an effective but rather generic model for chiral SOTIs [7]:

$$H(\mathbf{k}) = \left(m + b\sum_{i=x,y,z} \cos k_i\right)\tau_3 + v\sum_{i=x,y,z} \sin k_i \sigma_i \tau_1 + \Delta(\cos k_x - \cos k_y)\tau_2, \tag{4}$$

where $\mathbf{k} = (k_x, k_y, k_z)$ is the wave vector, $\boldsymbol{\tau} = (\tau_1, \tau_2, \tau_3)$ and $\boldsymbol{\sigma} = (\sigma_x, \sigma_y, \sigma_z)$ are Pauli matrices acting on orbital and spin spaces, respectively, and m, b, v, and Δ are model parameters. Without loss of generality, we set the lattice constant and the velocity v to unity. When $1 < |m/b| < 3$ and $\Delta = 0$, the model describes 3D topological insulators with gapless surface states protected by time-reversal symmetry $\mathcal{T}$ [72]. A finite Δ breaks time-reversal and $\mathcal{C}_4$ rotation symmetries individually. Thus, it opens gaps in the surface states. However, Δ preserves the combined symmetry $\mathcal{C}_4\mathcal{T}$. As a result, the gaps depend on the surface orientation, leading to gapless chiral hinge states localized at the hinges connecting adjacent surfaces.

We consider the orbital effect of $\mathbf{B}$ via the Peierls replacement $T_{ij} \to T_{ij}\exp(2\pi i \int_{r_i}^{r_j} d\mathbf{r}\cdot\mathbf{A}/\phi_0)$, where T_{ij} is the hopping amplitude from sites r_i to r_j, and $\phi_0 = h/e$ is flux quantum. The vector potential is chosen in the gauge $\mathbf{A} = B(0, 0, y\cos\theta - x\sin\theta)$ for concreteness. For simplicity, we model the leads (with a low-energy quadratic dispersion) by a standard cubic lattice and assume only a few transport channels in both leads such that finite reflection and transmission for the hinge channels are generated at the interfaces. Under these considerations, we calculate the two-terminal conductance numerically, employing the standard Landauer-Büttiker approach [64–66] in combination with lattice Green functions [62]. We emphasize that our main results illustrated below remain qualitatively the same if we choose other models for the SOTI or the leads.

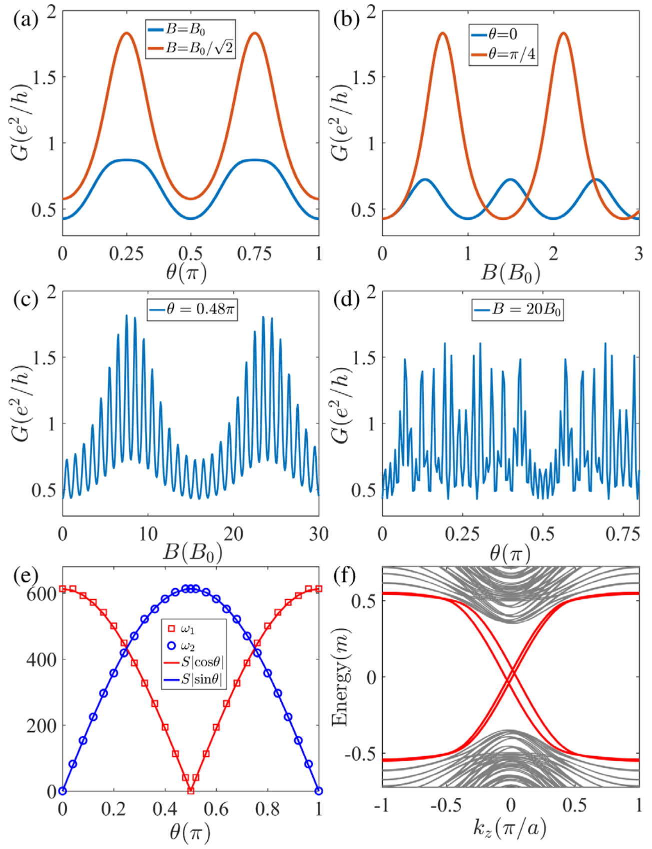

FIG. 2. (a) Conductance G as a function of field direction θ at field strengths $B = B_0$ and $B_0/\sqrt{2}$, respectively. (b) G as a function of B for $\theta = 0$ and $\pi/4$, respectively. (c) Particular beating patterns with varying B at $\theta = 0.48\pi$. (d) Beating patterns with varying θ at a large field strength $B = 20B_0$. (e) Extracted frequencies (square and circle dots) as a function of θ. (f) Low-energy spectrum of the SOTI with $B = 2B_0$ and $\theta = 0.15\pi$. Other parameters: $L = 60a$, $W_x = W_y = 12a$, $m = 2$, $b = -1$, $v = 1$, $\Delta = 1$, and $E_F = 0.002$.

Quantum interference pattern.—Now, we analyze the dependence of G on $\mathbf{B}$, combining the general scattering theory and concrete numerical simulations. First, Eq. (2) implies an oscillation pattern of G with respect to field direction θ. This is confirmed by our numerical results in Fig. 2(a), which shows $G(\theta)$ as a function of θ for given B. For weak fields $B \le B_0$, $G(\theta)$ is approximately a sinusoidal function of θ. For strong fields $B > B_0$, the number of conductance peaks and valleys increases with increasing B [Fig. 1(c)]. Second, Eq. (2) also indicates an oscillation pattern of G with respect to B, which is again fully confirmed by our numerical simulations. When $\mathbf{B}$ is in the x or y direction or at the specific angle $\theta \in \Theta_X \equiv \{\pm\alpha_0, \pi \pm \alpha_0\}$ with $\alpha_0 \equiv \arctan(W_x/W_y)$, $G(B)$ exhibits simple oscillations with a single frequency [Fig. 2(b)]. Generally, $G(B)$ takes maximal or minimal values when the interference loop encloses half a flux quantum $\phi_0/2$. For $\theta = 0$, $G(B)$ takes maximal values at odd multiples of $B_0/2$. The oscillation amplitude is relatively smaller since only two of the four loops enclose $\phi_0/2$. For $\theta = \pi/4$,

$G(B)$ takes maximal values at instead odd multiples of $B_0/\sqrt{2}$, where all interference loops enclose $\phi_0/2$. These features signify the interferometer formed by hinge states being of the Fabry-Pérot type, as we further explain below.

Notably, there exist beating patterns in $G(B)$. When $\mathbf{B}$ deviates away from the directions $\theta = n\pi/2$ and Θ_X, the beating patterns are clearly observed [Fig. 2(c)]. By performing discrete Fourier transformation, we extract precisely two frequencies: ω_1 and ω_2. These frequencies depend strongly on θ [dotted lines in Fig. 2(e)]. Explicitly, we find that they can be well described by $\omega_1 = LW_y|\cos\theta| = |\phi|/B$ and $\omega_2 = LW_x|\sin\theta| = |\varphi|/B$, respectively [solid lines in Fig. 2(e)]. They correspond exactly to the two AB phases, in excellent agreement with the results obtained from our scattering-matrix analysis. When $\theta = n\pi/2$, only one of the two frequencies survives. When $\theta \in \Theta_X$, the two frequencies become identical. In both cases, the beating behavior disappears. Similarly, $G(\theta)$ also shows beatinglike patterns with respect to θ with peaks and valleys for large fields $B \gg B_0$ [Fig. 2(d)]. This direction-induced beating behavior is another manifestation of the two AB phases.

Higher-order Fabry-Pérot interference.—Next we clarify in which sense the interference pattern is of the higher-order Fabry-Pérot type. The two frequencies in the beating patterns correspond to the projections of two areas enclosed by the interference loops in the plane normal to the field direction. As rotating $\mathbf{B}$ in the $x-y$ plane, the frequencies match the effective areas $LW_y|\cos\theta|$ and $LW_x|\sin\theta|$ of the front and top surfaces quite well [Fig. 2(e)]. This result indicates that adjacent hinge states with opposite chirality form interference loops and hence the interference is of the Fabry-Pérot type. The interference loops are made of chiral hinge states that are protected by higher-order topology and exist in 3D space. This further defines a higher-order Fabry-Pérot interferometer. Such an interferometer has several unique features in the interference pattern, as shown in Fig. 2(e): (i) It generally shows multiple linked frequencies that depend strongly on field direction θ; (ii) When rotating $\mathbf{B}$, there are always some frequencies increasing whereas the other ones are decreasing; (iii) At certain θ, two of the frequencies become identical. For the setup considered in Fig. 1(a), the two frequencies coincide at $\theta \in \Theta_X$ [73].

The mechanism behind the interferometer can be better understood by analyzing the hinge-state spectrum under $\mathbf{B}$. In the absence of $\mathbf{B}$, the hinge-state spectrum is double degenerated and linear in k_z, i.e., $\pm v k_z$. Applying $\mathbf{B}$ gives rise to a spatially varying vector potential $\mathbf{A}$, thus shifting the linear spectrum. Note that the hinge states are localized at different hinges of the SOTI. Under the chosen gauge, the spectrum is split as $+v(k_z \pm \delta k_1^z)$ and $-v(k_z \pm \delta k_2^z)$, where the splittings are $\delta k_1^z = BW_x \sin(\theta - \alpha_0)/2$ and $\delta k_2^z = BW_y \cos(\theta + \alpha_0)/2$ [62]. Thus, the hinge states acquire finite wave numbers even for vanishing Fermi energy [Fig. 2(f)]. When propagating along hinge channels of the interferometer, electrons pick up phase shifts $\pm\delta k_{1/2}^z L$. These phase shifts turn out to be the AB phases stemming from the magnetic flux enclosed by each loop, i.e., $\phi, \varphi = (\delta k_1^z \pm \delta k_2^z)L$. At special θ, for instance, $\theta = \alpha_0$ or $\alpha_0 + \pi$, one kind of splitting vanishes whereas the other one remains finite, i.e., $\delta k_1^z = 0$ and $\delta k_2^z \neq 0$. In these cases, the interference pattern reduces to a single frequency.

Experimental implementation.—Our higher-order interferometer with the aforementioned main features, such as the beating patterns and field-direction dependent frequencies, can be implemented in many candidates of magnetic SOTIs, e.g., $\mathrm{EuIn_2As_2}$ [74–77], $\mathrm{MnBi_{2n}Te_{3n+1}}$ [69,71,78–81], and Sm-doped $\mathrm{Bi_2Se_3}$ [82]. These transport features only rely on the existing chiral hinge states inside the bulk and side surface insulating gap. They are not sensitive to the details of materials (e.g., model parameters). For SOTIs with D_3 symmetry [83], there are three pairs of chiral hinge states within an insulating gap that is up to tens of meV in prominent candidate materials [71,74,78–80]. Similar to $\mathcal{C}_4\mathcal{T}$-symmetric SOTIs, we find that the hinge-state spectra are split by different amounts of momenta under $\mathbf{B}$ [Fig. 3(a)]. When implementing such SOTIs in the interferometer setup, we can observe the same main features that we discussed above in the magnetoconductance. Explicitly, the conductance exhibits beating patterns with three frequencies in general. These frequencies depend sensitively and periodically on field direction θ with period $\pi/3$ [Fig. 3(b)]. With rotating θ, for instance, from $(0, \pi/6)$, two frequencies increase whereas the other one decreases. At $\theta = 0$ or $\pi/6$, two of the frequencies coincide. Moreover, the third one vanishes at $\theta = 0$. Thus, a single and two frequencies can be observed at $\theta = 0$ and $\pi/6$, respectively.

We note that although the Zeeman effect of magnetic fields affects the gaps opened at the side surfaces of SOTIs, it does not alter the energy bands of hinge states. We show this

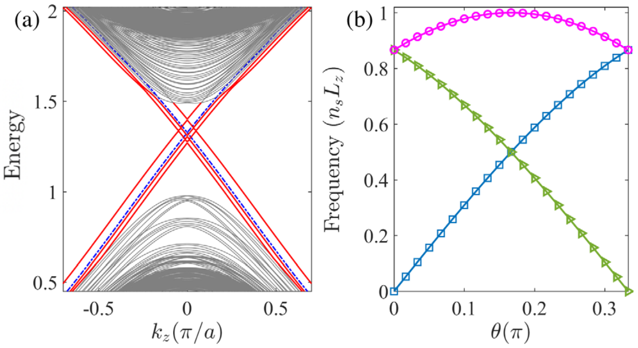

FIG. 3. (a) Low-energy spectrum of D_3 symmetric SOTIs on a hexagonal prism under $\mathbf{B}$. The hinge states are indicated by the red solid lines. Degenerated hinge states (dashed blue lines) in the absence of $\mathbf{B}$ are plotted for comparison. (b) The corresponding three frequencies as functions of θ. Details about the lattice model and the parameters can be found in the SM [62].

analytically and numerically based on the generic magnetic SOTI model [62]. Thus, we expect our higher-order interferometer based on the chiral hinge states of SOTIs to be not sensitive to the Zeeman effect as long as the latter is small and does not close the surface gaps. We next discuss some length and energy scales of experimental relevance [62]. Typically, the localization length of hinge states is of the order of several nanometers [62]. For candidate materials (e.g., $\mathrm{MnBi}_{2n}\mathrm{Te}_{3n+1}$) fabricated in a clean way, we could expect a phase coherence length of the order of 1 μm at low temperatures [51,71]. To avoid finite size effects and retain quantum coherence, we consider, for instance, a sample with experimentally feasible dimensions: $W_{x/y} \sim 100$ nm and $L \sim 1$ μm in a slab geometry. Then, the field strength to reach a flux quantum threading the surfaces is estimated as $B_0 \simeq 0.006$ T. Therefore, we argue that the particular oscillation pattern of the conductance can be observed in magnetic fields far below the in-plane saturation fields of candidate SOTIs (e.g., $\simeq 1$ T in $\mathrm{MnBi}_{2n}\mathrm{Te}_{3n+1}$ [80] and $\mathrm{EuIn}_2\mathrm{As}_2$ [76]). Moreover, we study the influence of disorder and dephasing due to environmental noises [62]. Remarkably, we find that the oscillation patterns persist under moderate disorder and weak dephasing. This further supports the robustness of our proposal.

Conclusion.—We have proposed a higher-order Fabry-Pérot interferometer based on chiral hinge states of SOTIs. Because of higher-order topology, this interferometer is intrinsically 3D and features particular beating patterns in the conductance by tuning strength or direction of an applied magnetic field. Our results provide feasible transport signatures and shed light on potential applications of hinge states in HOTIs.

This work was supported by the DFG (SPP1666 and SFB1170 “ToCoTronics”), the Würzburg-Dresden Cluster of Excellence ct.qmat, EXC2147, project-id 390858490, and the Elitenetzwerk Bayern Graduate School on “Topological Insulators.” J. L. acknowledges support by NSFC under Grant No. 11774317.

---

[*] Corresponding author.
changan.li@uni-wuerzburg.de

[†] Corresponding author.
song-bo.zhang@uni-wuerzburg.de

[1] W. A. Benalcazar, B. A. Bernevig, and T. L. Hughes, Quantized electric multipole insulators, Science **357**, 61 (2017).

[2] W. A. Benalcazar, B. A. Bernevig, and T. L. Hughes, Electric multipole moments, topological multipole moment pumping, and chiral hinge states in crystalline insulators, Phys. Rev. B **96**, 245115 (2017).

[3] R.-J. Slager, L. Rademaker, J. Zaanen, and L. Balents, Impurity-bound states and Green’s function zeros as local signatures of topology, Phys. Rev. B **92**, 085126 (2015).

[4] Y. Peng, Y. Bao, and F. von Oppen, Boundary Green functions of topological insulators and superconductors, Phys. Rev. B **95**, 235143 (2017).

[5] J. Langbehn, Y. Peng, L. Trifunovic, F. von Oppen, and P. W. Brouwer, Reflection-Symmetric Second-Order Topological Insulators and Superconductors, Phys. Rev. Lett. **119**, 246401 (2017).

[6] Z. Song, Z. Fang, and C. Fang, $(d-2)$-Dimensional Edge States of Rotation Symmetry Protected Topological States, Phys. Rev. Lett. **119**, 246402 (2017).

[7] F. Schindler, A. M. Cook, M. G. Vergniory, Z. Wang, S. S. P. Parkin, B. A. Bernevig, and T. Neupert, Higher-order topological insulators, Sci. Adv. **4**, eaat0346 (2018).

[8] M. Geier, L. Trifunovic, M. Hoskam, and P. W. Brouwer, Second-order topological insulators and superconductors with an order-two crystalline symmetry, Phys. Rev. B **97**, 205135 (2018).

[9] M. Ezawa, Higher-Order Topological Insulators and Semimetals on the Breathing Kagome and Pyrochlore Lattices, Phys. Rev. Lett. **120**, 026801 (2018).

[10] E. Khalaf, Higher-order topological insulators and superconductors protected by inversion symmetry, Phys. Rev. B **97**, 205136 (2018).

[11] M. J. Park, Y. Kim, G. Y. Cho, and S. B. Lee, Higher-Order Topological Insulator in Twisted Bilayer Graphene, Phys. Rev. Lett. **123**, 216803 (2019).

[12] L. Trifunovic and P. W. Brouwer, Higher-Order Bulk-Boundary Correspondence for Topological Crystalline Phases, Phys. Rev. X **9**, 011012 (2019).

[13] Y. You, T. Devakul, F. J. Burnell, and T. Neupert, Higher-order symmetry-protected topological states for interacting bosons and fermions, Phys. Rev. B **98**, 235102 (2018).

[14] T. Hirosawa, S. A. Díaz, J. Klinovaja, and D. Loss, Magnonic Quadrupole Topological Insulator in Antiskyrmion Crystals, Phys. Rev. Lett. **125**, 207204 (2020).

[15] S. Franca, J. van den Brink, and I. C. Fulga, An anomalous higher-order topological insulator, Phys. Rev. B **98**, 201114(R) (2018).

[16] G. van Miert and C. Ortix, Higher-order topological insulators protected by inversion and rotoinversion symmetries, Phys. Rev. B **98**, 081110(R) (2018).

[17] F. Schindler, Z. Wang, M. G. Vergniory, A. M. Cook, A. Murani, S. Sengupta *et al.*, Higher-order topology in bismuth, Nat. Phys. **14**, 918 (2018).

[18] S. Imhof, C. Berger, F. Bayer, J. Brehm, L. W. Molenkamp, T. Kiessling *et al.*, Topolectrical-circuit realization of topological corner modes, Nat. Phys. **14**, 925 (2018).

[19] C. W. Peterson, W. A. Benalcazar, T. L. Hughes, and G. Bahl, A quantized microwave quadrupole insulator with topologically protected corner states, Nature (London) **555**, 346 (2018).

[20] M. Serra-Garcia, V. Peri, R. Süsstrunk, O. R. Bilal, T. Larsen, L. G. Villanueva, and S. D. Huber, Observation of a phononic quadrupole topological insulator, Nature (London) **555**, 342 (2018).

[21] X.-D. Chen, W.-M. Deng, F.-L. Shi, F.-L. Zhao, M. Chen, and J.-W. Dong, Direct Observation of Corner States in Second-Order Topological Photonic Crystal Slabs, Phys. Rev. Lett. **122**, 233902 (2019).

[22] Y. Peng and G. Refael, Floquet Second-Order Topological Insulators from Nonsymmorphic Space-Time Symmetries, Phys. Rev. Lett. **123**, 016806 (2019).

[23] A. K. Ghosh, G. C. Paul, and A. Saha, Higher order topological insulator via periodic driving, Phys. Rev. B **101**, 235403 (2020).

[24] A. El Hassan, F. K. Kunst, A. Moritz, G. Andler, E. J. Bergholtz, and M. Bourennane, Corner states of light in photonic waveguides, Nat. Photonics **13**, 697 (2019).

[25] X. Ni, M. Weiner, A. Alù, and A. B. Khanikaev, Observation of higher-order topological acoustic states protected by generalized chiral symmetry, Nat. Mater. **18**, 113 (2019).

[26] B.-Y. Xie, G.-X. Su, H.-F. Wang, H. Su, X.-P. Shen, P. Zhan, M.-H. Lu, Z.-L. Wang, and Y.-F. Chen, Visualization of Higher-Order Topological Insulating Phases in Two-Dimensional Dielectric Photonic Crystals, Phys. Rev. Lett. **122**, 233903 (2019).

[27] Y. Qi, C. Qiu, M. Xiao, H. He, M. Ke, and Z. Liu, Acoustic Realization of Quadrupole Topological Insulators, Phys. Rev. Lett. **124**, 206601 (2020).

[28] Z. Wang, B. J. Wieder, J. Li, B. Yan, and B. A. Bernevig, Higher-Order Topology, Monopole Nodal Lines, and The Origin of Large Fermi Arcs in Transition Metal Dichalcogenides $X\mathrm{Te}_2$ ($X = \mathrm{Mo, W}$), Phys. Rev. Lett. **123**, 186401 (2019).

[29] D. Călugăru, V. Juričić, and B. Roy, Higher-order topological phases: A general principle of construction, Phys. Rev. B **99**, 041301(R) (2019).

[30] A. L. Szabó, R. Moessner, and B. Roy, Strain-engineered higher-order topological phases for spin-$3/2$ Luttinger fermions, Phys. Rev. B **101**, 121301(R) (2020).

[31] X.-L. Sheng, C. Chen, H. Liu, Z. Chen, Z.-M. Yu, Y. X. Zhao, and S. A. Yang, Two-Dimensional Second-Order Topological Insulator in Graphdiyne, Phys. Rev. Lett. **123**, 256402 (2019).

[32] C.-A. Li and S.-S. Wu, Topological states in generalized electric quadrupole insulators, Phys. Rev. B **101**, 195309 (2020).

[33] C.-A. Li, B. Fu, Z.-A. Hu, J. Li, and S.-Q. Shen, Topological Phase Transitions in Disordered Electric Quadrupole Insulators, Phys. Rev. Lett. **125**, 166801 (2020).

[34] H. Li and K. Sun, Pfaffian Formalism for Higher-Order Topological Insulators, Phys. Rev. Lett. **124**, 036401 (2020).

[35] B. A. Levitan and T. Pereg-Barnea, Second-order topological insulator under strong magnetic field: Landau levels, Zeeman effect, and magnetotransport, Phys. Rev. Research **2**, 033327 (2020).

[36] X. Zhu, Tunable Majorana corner states in a two-dimensional second-order topological superconductor induced by magnetic fields, Phys. Rev. B **97**, 205134 (2018).

[37] Y. Volpez, D. Loss, and J. Klinovaja, Second-Order Topological Superconductivity in π-junction Rashba Layers, Phys. Rev. Lett. **122**, 126402 (2019).

[38] X.-W. Luo and C. Zhang, Higher-Order Topological Corner States Induced by Gain and Loss, Phys. Rev. Lett. **123**, 073601 (2019).

[39] R.-X. Zhang, W. S. Cole, X. Wu, and S. Das Sarma, Higher-Order Topology and Nodal Topological Superconductivity in Fe(Se,Te) Heterostructures, Phys. Rev. Lett. **123**, 167001 (2019).

[40] R.-X. Zhang, Y.-T. Hsu, and S. Das Sarma, Higher-order topological Dirac superconductors, Phys. Rev. B **102**, 094503 (2020).

[41] M. Ezawa, Braiding of Majorana-like corner states in electric circuits and its non-Hermitian generalization, Phys. Rev. B **100**, 045407 (2019).

[42] S.-B. Zhang, A. Calzona, and B. Trauzettel, All-electrically tunable networks of Majorana bound states, Phys. Rev. B **102**, 100503(R) (2020).

[43] S.-B. Zhang, W. B. Rui, A. Calzona, S.-J. Choi, A. P. Schnyder, and B. Trauzettel, Topological and holonomic quantum computation based on second-order topological superconductors, Phys. Rev. Research **2**, 043025 (2020).

[44] T. E. Pahomi, M. Sigrist, and A. A. Soluyanov, Braiding Majorana corner modes in a second-order topological superconductor, Phys. Rev. Research **2**, 032068(R) (2020).

[45] R. Queiroz and A. Stern, Splitting the Hinge Mode of Higher-Order Topological Insulators, Phys. Rev. Lett. **123**, 036802 (2019).

[46] C.-Z. Li, A.-Q. Wang, C. Li, W.-Z. Zheng, A. Brinkman, D.-P. Yu, and Z.-M. Liao, Reducing Electronic Transport Dimension to Topological Hinge States by Increasing Geometry Size of Dirac Semimetal Josephson Junctions, Phys. Rev. Lett. **124**, 156601 (2020).

[47] Y.-B. Choi, Y. Xie, C.-Z. Chen, J. Park, S.-B. Song, J. Yoon *et al.*, Evidence of higher-order topology in multilayer WTe_2 from Josephson coupling through anisotropic hinge states, Nat. Mater. **19**, 974 (2020).

[48] Y. Aharonov and D. Bohm, Significance of electromagnetic potentials in the quantum theory, Phys. Rev. **115**, 485 (1959).

[49] J. H. Bardarson, P. W. Brouwer, and J. E. Moore, Aharonov-Bohm Oscillations in Disordered Topological Insulator Nanowires, Phys. Rev. Lett. **105**, 156803 (2010).

[50] Y. Zhang and A. Vishwanath, Anomalous Aharonov-Bohm Conductance Oscillations from Topological Insulator Surface States, Phys. Rev. Lett. **105**, 206601 (2010).

[51] H. Peng, K. Lai, D. Kong, S. Meister, Y. Chen, X.-L. Qi, S.-C. Zhang, Z.-X. Shen, and Y. Cui, Aharonov-Bohm interference in topological insulator nanoribbons, Nat. Mater. **9**, 225 (2010).

[52] J. H. Bardarson and J. E. Moore, Quantum interference and Aharonov–Bohm oscillations in topological insulators, Rep. Prog. Phys. **76**, 056501 (2013).

[53] A. R. Akhmerov, J. Nilsson, and C. W. J. Beenakker, Electrically Detected Interferometry of Majorana Fermions in a Topological Insulator, Phys. Rev. Lett. **102**, 216404 (2009).

[54] L. Fu and C. L. Kane, Probing Neutral Majorana Fermion Edge Modes with Charge Transport, Phys. Rev. Lett. **102**, 216403 (2009).

[55] J. Li, G. Fleury, and M. Büttiker, Scattering theory of chiral Majorana fermion interferometry, Phys. Rev. B **85**, 125440 (2012).

[56] C.-A. Li, J. Li, and S.-Q. Shen, Majorana-Josephson interferometer, Phys. Rev. B **99**, 100504(R) (2019).

[57] L.-X. Wang, C.-Z. Li, D.-P. Yu, and Z.-M. Liao, Aharonov-Bohm oscillations in Dirac semimetal $\mathrm{Cd_3As_2}$ nanowires, Nat. Commun. **7**, 10769 (2016).

[58] Note that our predictions are more robust than a quantized conductance stemming from the hinge states at zero magnetic field. The reason is that our magnetotransport results profit from a coupling of the hinge states before they

enter the leads. In contrast, the quantized conductance at zero field is reduced by such coupling.

[59] M. Büttiker, Scattering theory of current and intensity noise correlations in conductors and wave guides, Phys. Rev. B **46**, 12485 (1992).

[60] Y. V. Nazarov and Y. M. Blanter, *Quantum Transport: Introduction to Nanoscience* (Cambridge University Press, Cambridge, England, 2006).

[61] J. Maciejko, E.-A. Kim, and X.-L. Qi, Spin Aharonov-Bohm effect and topological spin transistor, Phys. Rev. B **82**, 195409 (2010).

[62] See Supplemental Material, which includes Refs. [63–71], at http://link.aps.org/supplemental/10.1103/PhysRevLett.127.026803 for details.

[63] S.-B. Zhang and B. Trauzettel, Detection of second-order topological superconductors by Josephson junctions, Phys. Rev. Research **2**, 012018(R) (2020).

[64] R. Landauer, Electrical resistance of disordered one-dimensional lattices, Philos. Mag. **21**, 863 (1970).

[65] M. Büttiker, Four-Terminal Phase-Coherent Conductance, Phys. Rev. Lett. **57**, 1761 (1986).

[66] S. Datta, *Electronic Transport in Mesoscopic Systems* (Cambridge University Press, Cambridge, England, 1995).

[67] A. MacKinnon, The calculation of transport properties and density of states of disordered solids, Z. Phys. B **59**, 385 (1985).

[68] C. W. Groth, M. Wimmer, A. R. Akhmerov, and X. Waintal, Kwant: A software package for quantum transport, New J. Phys. **16**, 063065 (2014).

[69] R.-X. Zhang, F. Wu, and S. Das Sarma, Möbius Insulator and Higher-Order Topology in $\mathrm{MnBi}_{2n}\mathrm{Te}_{3n+1}$, Phys. Rev. Lett. **124**, 136407 (2020).

[70] H. Jiang, S. Cheng, Q.-F. Sun, and X. C. Xie, Topological Insulator: A New Quantized Spin Hall Resistance Robust to Dephasing, Phys. Rev. Lett. **103**, 036803 (2009).

[71] M. M. Otrokov *et al.*, Prediction and observation of an antiferromagnetic topological insulator, Nature (London) **576**, 416 (2019).

[72] H. Zhang, C. X. Liu, X. L. Qi, X. Dai, Z. Fang, and S. C. Zhang, Topological insulators in $\mathrm{Bi}_2\mathrm{Se}_3$, $\mathrm{Bi}_2\mathrm{Te}_3$ and $\mathrm{Sb}_2\mathrm{Te}_3$ with a single Dirac cone on the surface, Nat. Phys. **5**, 438 (2009).

[73] We also consider a geometry with lower symmetry—for instance, the cross section is a trapezoid; see the SM.

[74] Y. Xu, Z. Song, Z. Wang, H. Weng, and X. Dai, Higher-Order Topology of the Axion Insulator $\mathrm{EuIn}_2\mathrm{As}_2$, Phys. Rev. Lett. **122**, 256402 (2019).

[75] T. Sato, Z. Wang, D. Takane, S. Souma, C. Cui, Y. Li *et al.*, Signature of band inversion in the antiferromagnetic phase of axion insulator candidate $\mathrm{EuIn}_2\mathrm{As}_2$, Phys. Rev. Research **2**, 033342 (2020).

[76] Y. Zhang, K. Deng, X. Zhang, M. Wang, Y. Wang, C. Liu *et al.*, In-plane antiferromagnetic moments and magnetic polaron in the axion topological insulator candidate $\mathrm{EuIn}_2\mathrm{As}_2$, Phys. Rev. B **101**, 205126 (2020).

[77] S. Regmi, M. M. Hosen, B. Ghosh, B. Singh, G. Dhakal, C. Sims *et al.*, Temperature-dependent electronic structure in a higher-order topological insulator candidate $\mathrm{EuIn}_2\mathrm{As}_2$, Phys. Rev. B **102**, 165153 (2020).

[78] X. Wu *et al.*, Distinct Topological Surface States on The Two Terminals of $\mathrm{MnBi}_4\mathrm{Te}_7$, Phys. Rev. X **10**, 031013 (2020).

[79] R. C. Vidal *et al.*, Topological Electronic Structure and Intrinsic Magnetization in $\mathrm{MnBi}_4\mathrm{Te}_7$: A $\mathrm{Bi}_2\mathrm{Te}_3$ Derivative with a Periodic Mn Sublattice, Phys. Rev. X **9**, 041065 (2019).

[80] C. Hu, K. N. Gordon, P. Liu, J. Liu, X. Zhou, P. Hao *et al.*, A van der Waals antiferromagnetic topological insulator with weak interlayer magnetic coupling, Nat. Commun. **11**, 97 (2020).

[81] R. Chen, S. Li, H.-P. Sun, Y. Zhao, H.-Z. Lu, and X. C. Xie, Using nonlocal surface transport to identify the axion insulator, Phys. Rev. B **103**, L241409 (2021).

[82] C. Yue, Y. Xu, Z. Song, H. Weng, Y.-M. Lu, C. Fang, and X. Dai, Symmetry-enforced chiral hinge states and surface quantum anomalous Hall effect in the magnetic axion insulator $\mathrm{Bi}_{2-x}\mathrm{Sm}_x\mathrm{Se}_3$, Nat. Phys. **15**, 577 (2019).

[83] Note that, for pedagogical reasons, we have discussed the cases of SOTIs with $\mathcal{C}_4\mathcal{T}$ symmetry before. While some of the known SOTIs have D_3 symmetry.